THESIS FOR THE DEGREE OF LICENTIATE OF PHILOSOPHY

CO oxidation over platinum-ceria catalysts

Structural dynamics and reaction mechanisms

Mengqiao Di

CHALMERS

Department of Chemistry and Chemical Engineering
CHALMERS UNIVERSITY OF TECHNOLOGY
Göteborg, Sweden 2021

CO oxidation over platinum-ceria catalysts

Structural dynamics and reaction mechanisms

Mengqiao Di

Licentiatuppsatser vid Institutionen för kemi och kemiteknik

Chalmers tekniska högskola

Nr 2021:18

Department of Chemistry and Chemical Engineering

Chalmers University of Technology

SE-412 96 Göteborg

Telephone +46 31 772 1000

Typeset in LaTeX using the kaobook class

Printed by Chalmers Reproservice

Göteborg, Sweden 2021

CO oxidation over platinum-ceria catalysts
Structural dynamics and reaction mechanisms
Mengqiao Di
Department of Chemistry and Chemical Engineering
Chalmers University of Technology

Abstract

Catalytic oxidation of carbon monoxide (CO) continues to be important due to its wide applicability in emission control, in-door air cleaning, fuel cell efficiency enhancement, chemical feedstocks purification etc. The transportation sector emits most of the CO emissions. This is because modern powertrains and driving patterns result in exhausts with low temperatures at which the catalyst cannot operate efficiently. Thus, catalysts for CO oxidation needs to be developed as to be more active at low temperatures, ideally, even at ambient conditions. The metal oxide supported platinum catalyst is a practical choice thanks to its high robustness, i.e., resistance to sintering and deactivation by water, carbon dioxide and sulfur species. Although it has been extensively studied, the influence of chemical and structural dynamics on the catalytic activity under reaction conditions is still debated, especially for industrial catalysts.

This work aims at understanding the catalytic function of platinum highly dispersed onto ceria, which is a reducible support. The kinetic behaviours during catalytic extinction and reaction orders have been experimentally determined using a fixed-bed flow reactor. To explore the structure-function relationships, *operando* infrared and X-ray absorption spectroscopy have been used. Also, detailed reaction pathways have been simulated using kinetic Monte Carlo with kinetic parameters determined from *ab initio* calculations.

The CO oxidation kinetics for Pt/ceria is qualitatively different from that of reference Pt/alumina. The extinction profile for Pt/ceria catalyst exhibits a smooth decay in CO conversion rather than a stepwise drop as for the Pt/alumina catalyst. This is due to the two supports modifying the Pt particles differently as well as complementary reaction paths towards CO_2 facilitated by boundary sites only for the Pt/ceria catalyst. Furthermore, *operando* spectroscopy reveals that the Pt particles bind strongly with ceria showing an unaltered Pt-O bond distance of 2 Å during catalytic extinction. Although difficult to experimentally determine, charge transfer from Pt particles to ceria supplemented with reverse spillover of ceria lattice oxygen to the vicinity of Pt particles likely occur.

Keywords: CO oxidation; Platinum catalysts; *Operando* spectroscopy; XANES; EXAFS; DRIFTS

List of Publications

This thesis is based on the following appended papers, referred to by Roman numerals in the text:

I. Dynamics of small platinum particles obscured by support interactions

Mengqiao Di, Kerry Simmance, Andreas Schaefer, Yanyue Feng, Felix Hemmingsson, Magnus Skoglundh, David Thompsett, Lucy Idowu Ajakaiye Jensen, Sara Blomberg and Per-Anders Carlsson

In manuscript

II. Alternative reaction mechanisms for CO oxidation on Pt/CeO_2

Noemi Bosio, Mengqiao Di, Magnus Skoglundh, Per-Anders Carlsson and Henrik Grönbeck

In manuscript

My Contributions to the Publications

Paper I

Main author. Performed all the experimental work and data analysis except catalysts preparation and XRF.

Paper II

Co-author. Performed reaction order experiments.

Additional publications which are not included in the thesis:

Insight into hydrothermal aging effect on Pd sites over Pd/LTA and Pd/SSZ-13 as PNA and CO oxidation monolith catalysts

Aiyong Wang, Kristina Lindgren, Mengqiao Di, Diana Bernin, Per-Anders Carlsson, Mattias Thuvander and Louise Olsson

Applied Catalysis B: Environmental, 278 **(2020)**, 0926-3373

Explanation of anomalous rate capability enhancement by manganese oxide incorporation in carbon nanofiber electrodes for electrochemical capacitors

Qi Li, Volodymyr Kuzmenko, Mohammad Mazharul Haque, Mengqiao Di, Anderson David Smith, Per Lundgren and Peter Enoksson

Electrochimica Acta, 340 **(2020)**, 0013-4686

Acknowledgements

This research was carried out at Competence Centre for Catalysis (KCK), and Division of Applied Chemistry, Chalmers University of Technology, Göteborg, Sweden. Part of research was performed at beamline P65 at PETRA III, Deutsches Elektronen-Synchrotron (DESY) in Hamburg, Germany, and at Chalmers Materials Analysis Laboratory (CMAL). The beamtime is much appreciated and special thanks for all the technical support.

This work is financially supported by the Swedish Energy Agency and the member companies: AB Volvo, ECAPS AB, Johnson Matthey AB, Preem AB, Scania CV AB, Umicore AG & Co. KG and Volvo Car Corporation AB.

I would also like to thank:

My main supervisor Per-Anders Carlsson for all the constant support and guidance in the research. I appreciate all the feedback and opportunities from you to help me grow in this research field. Thank you so much for helping me go through this Licentiate and all the scientific discussions on different meetings.

My co-supervisor Henrik Grönbeck, and examiner Magnus Skoglundh for the stimulating and detailed discussions from different views. Your dedication towards science encourages me when I feel frustrated.

My collaborators, Noemi Bosio, Andreas Schaefer, Felix Hemmingsson, Aiyong Wang, Qi Li and Yanyue Feng. I enjoyed all the meetings and discussions with all of you. Special thanks to Felix Hemmingsson for the help of SGB3 maintenance. Thank the comments and questions from Andreas Schaefer that motivates me. Yanyue, thank you for the accompany and support sincerely.

David Thompsett and Kerry Simmance for all the constructive meetings, supportive input and creative ideas for my research.

Lasse Urholm, a big thank you for all the maintenance for the equipment.

Ghodsieh Isapour Toutizad, I really appreciated the travellings we have went together. Look forward to hearing more of your work from the field.

All my friends and colleagues in the department, I do appreciate all the great moments we have experienced together. I would like to thank Zhihang, Yifei, Yingxin, Zhe, Hao, Elyse, Chris, Ting, Peter, Carl-Robert, Alex and Guido.

Last but not the least, I would like to thank my boyfriend Xiao Lang for your love and tolerance to my bad temper and a lot of help in programming. I would like to express my sincerest gratitude to my parents for your constant support, love and encouragement over the years.

Mengqiao Di, Göteborg, October 2021

Contents

List of Figures

List of Tables

Notation and terms

$\tilde{\nu}_{br}^{CO}$(Pt)	bridge bonded CO adsorption on reduced Pt particles
$\tilde{\nu}_{lin}^{CO}$(Pt^0)	linear CO adsorption on reduced Pt particles
$\tilde{\nu}_{lin}^{CO}$(Pt^{2+})	linear CO adsorption on oxidised Pt particles
$\tilde{\nu}_{lin}^{CO}$($Pt^{\delta+}$)	linear CO adsorption on partially oxidised Pt particles
ADF	Annular Dark-Field
BF	Bright-Field
DF	Dark-Field
DFT	Density Functional Theory
DRIFTS	Diffuse Reflectance Infrared Fourier Transform Spectroscopy
EDX	Energy-Dispersive X-ray Spectroscopy
EELS	Electron Energy Loss Spectroscopy
EXAFS	Extended X-ray Absorption Fine Structure
FTIR	Fourier Transformed Infrared
HAADF	High-Angle Annular Dark-Field
HRTEM	High Resolution Transmission Electron Microscopy
IR	Infrared Spectroscopy
MARI	Most Abundant Reaction Intermediate
MFCs	Mass Flow Controllers
MS	Mass Spectrometry
PSD	Pore Size Distribution
SAD	Selected-Area Diffraction
SSA	Specific Surface Area
STEM	Scanning Transmission Electron Microscopy

STP	Standard Temperature and Pressure
TEM	Transmission Electron Microscopy
TEM/EDX	Transmission Electron Microscopy/Energy-dispersive X-ray spectroscopy
WLI	Whiteline Intensity
XAFS	X-ray Absorption Fine Structure
XANES	X-ray Absorption Near Edge Structure
XAS	X-ray Absorption Spectroscopy
XRD	X-ray diffraction

Introduction 1

1.1 Environmental catalysis

Since the industrial revolution until nowadays, fossil fuels have been exploited on a large scale. The energy from fossil fuels has been converted mainly by combustion as to be used in other forms. Although the main products of burning fossil fuels are carbon dioxide (CO_2) and water (H_2O), carbon monoxide (CO) can be easily formed upon incomplete combustion [1, 2], together with unburned hydrocarbons (HC), alcohols, and aldehydes. Also, sulfur oxides (SO_x) could be generated during the combustion due to fuel impurities and nitrogen oxides are formed when using air as oxidant.

These emissions cause environmental and health problems through increased global warming and air pollution. Both CO and NO_x are toxic to humans, even when encountered in concentrations around 150 ppm. This is due to their high affinity to hemoglobin in the blood. The most significant source of CO emissions, around 77%, is the transportation sector. Around 90% of the CO emissions come from the start-up of vehicles, often called the 'cold-start' period [3, 4]. Thus, vehicle emission standards (regulations) have been implemented such as the current European regulation named Euro VI. The standards regulate the specific emissions for certain pollutants (e.g., CO, NO_x and particulate matter) and the effective time duration. Recently, a more strict requirement for CO and NO_x emissions was proposed for a Euro VII regulation.

To meet the regulations, vehicles need to be equipped with catalytic converters for exhaust aftertreatment. The first definition of the catalysis phenomenon, expressing such reactions as to be driven by a catalytic force, was presented by Jöns Jacob Berzelius [5] in 1835. The next breakthrough was the Sabatier principle, in which Paul Sabatier [6] stated that the interaction between the catalyst and reactants/products should neither be too strong nor too weak for the catalytic reaction to proceed efficiently [7]. Later, the general expression of reaction rates, still used today, was derived by Irving Langmuir [8]. Today catalysis are frequently used for catalytic emission control and to increase other low emission power efficiency, e.g., fuel cells. Three-way catalytic converters (TWCs) have significantly decreased vehicle emissions of CO, HC, and NO_x at high temperatures. However, finding TWCs with full

functionality at low temperature, e.g., during vehicle start-up, is still challenging [9].

1.2 Catalytic CO oxidation

Catalysts for CO oxidation can be divided into several groups as shown in Figure 1.1. One example is the split into Au catalysts, platinum group metals (PGM), i.e., the noble metals Pt, Pd and Rh, w/wo support, supported alloy nanoparticles, and nanosized metal oxides. Au catalysts remain active at low temperatures, while sintering could occur at high temperatures. PGM exhibit high activity in the temperature range from 150 to 250 °C, and high resistance to sintering and deactivation of CO_2 and H_2O. After loading PGM on different supports (Al_2O_3, La_2O_3, TiO_2 and CeO_2, etc,.), a higher sulfur tolerance up to 1000 ppm is achieved, and the low-temperature activity is improved due to the interaction with supports. Some reducible supports play a vital role in stabilizing PGM to achieve single-atom catalysts, which show high activity at low temperatures (< 150 °C) [10, 11]. Higher thermal resistance and hydro-thermal durability are reached in order to be used under high engine loads, and periodic regeneration [12].

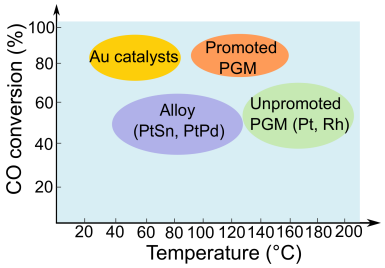

Figure 1.1: Scheme of catalytic performance of different catalysts for CO oxidation.

However, the cost and low availability of noble metals limit their applications. Thus, economically more viable catalysts have been considered, e.g., alloyed nanoparticles to lower the amount of PGM, and transition metals or metal oxides with spinel, hopcalite or perovskite structures. These could perform well for dry CO oxidation even at room temperature with high durability [13]. Recently, CuO and CeO_2 mixed oxides have been used as three-way catalysts thanks to their low cost and high resistance to H_2O, CO_2 and sulfur [14].

1.3 Objective

The objective of this thesis is to explore how CO oxidation proceeds on Pt/ceria catalysts under lean conditions and how the catalytic activity depends on the chemical state and structure of the catalysts. Several techniques and methods have been used for basic characterization and evaluation of catalyst performance. Also advanced *operando* spectroscopic catalyst characterisation and theoretical treatment of reaction kinetics and mechanisms have been employed to build understanding.

Background 2

2.1 Mechanisms for CO oxidation over Pt catalysts

Several mechanisms have been proposed for CO oxidation over Pt-based catalysts in the literature [15–20]. As first proposed by Langmuir, CO oxidation may proceed through a competitive adsorption of CO (associative) and O_2 (dissociative) followed by reaction between adsorbed CO and O forming CO_2 that desorbs fast. The corresponding elementary steps are expressed as:

$$\mathrm{CO\ (g)} + * \underset{k_1^-}{\overset{k_1^+}{\rightleftharpoons}} \mathrm{CO*} \tag{2.1}$$

$$\mathrm{O_2\ (g)} + 2* \underset{k_2^-}{\overset{k_2^+}{\rightleftharpoons}} 2\mathrm{O*} \tag{2.2}$$

$$\mathrm{O*} + \mathrm{CO*} \xrightarrow{k_r} \mathrm{CO_2\ (g)} + 2* \tag{2.3}$$

where * represents free sites, k_i^+, the adsorption rate constant and k_i^-, the desorption rate constant for different steps. The individual coverage under steady-state can be obtained with the assumption of $k_r \ll k_1^+$ and $k_r \ll k_2^+$.

$$\theta_{\mathrm{CO}} = K_1 P_{\mathrm{CO}} \theta_* \tag{2.6}$$

$$\theta_{\mathrm{O}} = \sqrt{K_2 P_{\mathrm{O_2}}}\,\theta_* \tag{2.7}$$

where $K_i = k_i^+ / k_i^-$ defines the equilibrium constant for species i. Considering CO as the Most Abundant Reaction Intermediate (MARI) at low temperatures and k_r as a rate-determining step (RDS), the reaction rate can be expressed in

$$r = k_r \frac{\sqrt{K_2 P_{\mathrm{O_2}}}}{K_1 P_{\mathrm{CO}}} \tag{2.8}$$

where k_r represents the reaction rate constant, leading to a reaction order of -1 for CO and 0.5 for O_2. This model has been reported for CO oxidation on Pt(111) surfaces at a high CO coverage [17, 18]. Nonetheless, another reaction order of around -1 for CO and 1 for O_2 has been measured for Pt(100) single crystal surfaces under stoichiometric conditions [20], and for 1.5 nm Pt particles on alumina under rich conditions [15]. This could also be explained by the Langmuir-Hinshelwood mechanism but taking CO-CO lateral

Herein the rate equations are:

$$\frac{d\theta_{\mathrm{CO}}}{dt} = k_1^+ p_{\mathrm{CO}} \theta_* - k_1^- \theta_{\mathrm{CO}} - k_r \theta_{\mathrm{CO}} \theta_{\mathrm{O}} \tag{2.4}$$

$$\frac{d\theta_{\mathrm{O}}}{dt} = 2k_2^+ p_{\mathrm{O_2}} \theta_*^2 - 2k_2^- \theta_{\mathrm{O_2}}^2 - k_r \theta_{\mathrm{CO}} \theta_{\mathrm{O}} \tag{2.5}$$

interactions into consideration [21]. Another possible model has been proposed by favoring a direct O_2 adsorption rather than O_2 dissociation [16] in the following reaction scheme:

$$CO(g) + * \underset{k_1^-}{\overset{k_1^+}{\rightleftharpoons}} CO* \tag{2.9}$$

$$O_2(g) + * \underset{k_2^-}{\overset{k_2^+}{\rightleftharpoons}} O_2* \tag{2.10}$$

$$O_2 * + CO* \overset{k_{r3}}{\rightarrow} CO_2(g) + O* \tag{2.11}$$

$$O * + CO* \overset{k_{r4}}{\rightarrow} CO_2(g) + 2* \tag{2.12}$$

The corresponding rate equations

$$\frac{d\theta_{CO}}{dt} = k_1^+ p_{CO}\theta_* - k_1^-\theta_{CO} - k_{r3}\theta_{CO}\theta_{O_2} - k_{r4}\theta_{CO}\theta_O \tag{2.13}$$

$$\frac{d\theta_{O_2}}{dt} = k_2^+ p_{O_2}\theta_* - k_2^-\theta_{O_2} - k_{r3}\theta_{CO}\theta_{O_2} \tag{2.14}$$

$$\frac{d\theta_O}{dt} = k_{r3}\theta_{CO}\theta_{O_2} - k_{r4}\theta_{CO}\theta_O \tag{2.15}$$

With the assumption of a low atomic oxygen coverage at steady-state ($k_{r3} \ll k_{r4}$) and CO as MARI, the coverage thus can be derived:

$$\theta_{CO} = \frac{K_1 P_{CO}}{1 + K_1 P_{CO}} \tag{2.16}$$

$$\theta_{O_2} = K_2 P_{O_2} \frac{1}{1 + K_1 P_{CO}} \tag{2.17}$$

In the end, the reaction rate is given by:

$$r = k_{r3} \frac{\sqrt{K_2 P_{O_2}}}{K_1 P_{CO}} \tag{2.18}$$

where it provides the reaction order -1 for CO and 1 for O_2. Moreover, the Mars-van-Krevelen mechanism was suggested by considering a reaction by consuming lattice oxygen from the oxide support as a RDS. Non-competitive adsorption of CO and O_2 on the Pt particles and oxide, respectively [22]. This model has been typically applied for Pt/ceria systems [15, 23] in a way:

$$CO(g) + *_1 \underset{k_1^-}{\overset{k_1^+}{\rightleftharpoons}} CO*_1 \tag{2.19}$$

$$O_2(g) + *_2 \underset{k_2^-}{\overset{k_2^+}{\rightleftharpoons}} O_2*_2 \tag{2.20}$$

$$O_2 *_2 + CO*_1 \overset{k_{r3}}{\rightarrow} CO_2(g) + O *_2 + *_1 \tag{2.21}$$

$$O *_2 + CO*_1 \overset{k_{r4}}{\rightarrow} CO_2(g) + *_1 + *_2 \tag{2.22}$$

The time-dependent rate equations:

$$\frac{d\theta_{CO}}{dt} = k_1^+ p_{CO}\theta_{*1} - k_1^-\theta_{CO} - k_{r3}\theta_{CO}\theta_{O_2} - k_{r4}\theta_{CO}\theta_O \tag{2.23}$$

$$\frac{d\theta_{O_2}}{dt} = k_2^+ p_{O_2}\theta_{*2} - k_2^-\theta_{O_2} - k_{r3}\theta_{CO}\theta_{O_2} \tag{2.24}$$

$$\frac{d\theta_O}{dt} = k_{r3}\theta_{CO}\theta_{O_2} - k_{r4}\theta_{CO}\theta_O \tag{2.25}$$

We assume no competition between CO and O_2 at steady-state,

then we obtain:

$$\theta_{\mathrm{CO}} = \frac{K_1 P_{\mathrm{CO}}}{1 + K_1 P_{\mathrm{CO}}} \tag{2.26}$$

$$\theta_{\mathrm{O_2}} = \frac{K_2 P_{\mathrm{O_2}}}{1 + K_2 P_{\mathrm{O_2}}} \tag{2.27}$$

$$\theta_O = \frac{k_{r3}}{k_{r4}} \frac{K_2 P_{\mathrm{O_2}}}{1 + K_2 P_{\mathrm{O_2}}} \tag{2.28}$$

Under the assumption of Eq. 2.21 as RDS, the reaction rate is:

$$r \approx k_{r3} \tag{2.29}$$

Eventually this leads to the reaction order of 0 for both CO and O_2.

2.2 Activity measurements

Kinetics gives the framework about chemical reaction rate and allows the study of reaction mechanisms about the rate expression and reaction pathway. Kinetics is from a macroscopic view to reveal the reaction rate concerning concentrations, pressures, and temperatures, and it provides a way to the microscopic view of the reacting molecules.

A kinetic study for a fixed-bed reactor needs to be performed in the kinetically controlled regime, where a typical experiment is conducted with a low conversion. Still, it needs to to exclude the possibility of internal and external diffusion examined by Weisz-Prater criterion and Mears' criterion, respectively [24], in below:

$$C_{\mathrm{wp}} = \frac{r_{\mathrm{obs}} \rho_c R_p^2}{D_{\mathrm{eff}} C_s} \tag{2.30}$$

where r_{obs} is the observed reaction rate (mol/$\mathrm{kg_{cat}}$· s), and it can be calculated from:

$$r_{\mathrm{obs}} = q \frac{p_{\mathrm{CO}}}{RT} \frac{X_{\mathrm{CO}}}{m_{\mathrm{cat}}} \tag{2.31}$$

where q is the volumetric flow rate at room temperature ($\mathrm{m^3/s}$), p_{CO}, the CO partial pressure, R, the molar gas constant (8.314 J/(mol· K)), T, the temperature (K), m_{cat}, the mass of catalyst (kg), and X_{CO}, the conversion. X_{CO} can be expressed as:

$$X_{\mathrm{CO}} = \frac{[\mathrm{CO}]_{\mathrm{in}} vol.\% - [\mathrm{CO}]_{\mathrm{out}} vol.\%}{[\mathrm{CO}]_{\mathrm{in}} vol.\%} \tag{2.32}$$

R_ρ is catalyst particle radius (m), ρ_c, the bulk density of catalyst ($\mathrm{kg/m^3}$) [1], ρ_b=(1-Φ)ρ_c (Φ is the porosity)[2], D_{eff}, the effective diffus-

C_{wp}= $\eta\phi_1$= $\frac{\text{Actual reaction rate}}{\text{A diffusion rate}}$
η defines as effectiveness factor
η= $\frac{\text{Observed reaction rate}}{\text{Reaction rate evaluated at } C_{As}}$
ϕ_1 represents the Thiele modulus for first order reaction
ϕ_1= $\frac{\text{Reaction order evaluated at } C_{As}}{\text{A diffusion rate}}$

1: ρ_c=$\frac{\text{Mass of catalyst}}{\text{Volume of catalyst}}$

2:

$$\Phi = \frac{\text{Volume of catalyst}}{\text{Reactor volume}}$$

$$\rho_b = \frac{\text{Mass of catalyst}}{\text{Reactor Volume}}$$

ivity (m^2/s), and C_s, the gas concentration at the external surface of the catalyst (mol/m^3). If $C_{wp} \ll 1$, one can neglect internal diffusion limitations. However, if $C_{wp} \gg 1$, it means the reaction is limited by internal diffusion. Further, it comes to determine the external mass transfer to catalyst surface by:

$$C_{mr} = \frac{r_{obs}\rho_b R_p n}{k_c C_{Ab}} \tag{2.33}$$

where n is the reaction order, C_{Ab}, the bulk reactant concentration (mol/m^3), and k_c, the mass transfer coefficient (m/s). When $C_{mr} < 0.15$, there is no external mass transfer limitations.

Additionally, the external mass transfer can be decided by comparing the estimated most significant concentration gradient ($\triangle C_{CO}$) with the bulk gas concentration (C^b_{CO}). $\triangle C_{CO}$ can be derived from the steady-state reaction rate for a fixed-bed reactor:

$$r = S_m k_c \triangle C_{CO} \tag{2.34}$$

where $S_m = \frac{3}{R_p \rho_c}$, and $k_c = \frac{ShD_{eff}}{2R_p}$. Thus:

$$\triangle C_{CO} = \frac{2rR_p^2\rho_c}{3ShD_{AB}} \tag{2.35}$$

where r can be substituted by r_{obs} using a reasonable low value for Sherwood number (Sh=1.5), and D_{AB} is the binary gas diffusivity (m^2/s). The amount of sample can be controlled by diluting with inert materials to keep isotherm, and any particle size should be eight times smaller than the tube diameter to avoid any bypass effects[3]. However, it should not be too small to suffer pressure drop problems. The internal heat transfer can be checked by Anderson criterion [34]:

$$\frac{\mid \triangle H_r \mid r_{obs}\rho_d R_p^2}{\lambda_e T_s} < 0.75\frac{RT_s}{E} \tag{2.36}$$

where λ_e is the effective thermal conductivity ($30\ J/(s \cdot m \cdot K)$), T_s, the catalyst surface temperature (K), and E, the true activation energy (J/mol). Moreover, turnover frequency (TOF) [4] shifts the focus from reaction to catalyst. It can be evaluated in terms of metal dispersion:

$$TOF(s^{-1}) = r_{obs} \cdot \frac{M_{Pt}}{X_{Pt}D_{Pt}} \tag{2.37}$$

where M_{Pt} is the molecular weight of Pt (g/mol), X_{Pt}, the Pt loading, and D_{Pt}, the Pt dispersion. Some kinetic data for CO oxidation over different supported Pt catalysts are summarized in Table 2.1.

3: reactants go through the tube without passing sample

4: molecules reacting per active site in unit time

Table 2.1: The reaction rate and Turnover frequency for CO oxidation at different temperatures for different platinum catalysts.

	Metal loading (wt%)	Reaction type	Temperature (°C)	Specific rate $\times 10^2$ ($mol_{CO} h^{-1} g^{-1}_{metal}$)	Turnover frequency$\times 10^2$ (s^{-1})	Reference
Pt/Al_2O_3	0.4	CO oxidation	150	/	0.36	Mergler et al. [25]
Pt_1/Al_2O_3	0.044	CO oxidation	140	6.66	0.3	Yang Lou et al. [26]
Pt_1/Al_2O_3	0.044	WGS	140	159.12	3.7	Yang Lou et al. [26]
Pt/Al_2O_3	1.5	CO oxidation	130	18	3.42	Liu et al. [27]
Pd/Al_2O_3	1.4	CO oxidation	135	10.8	2.35	Liu et al. [27]
Pt/SiO_2	5	CO oxidation	150	/	0.072	Mergler et al. [25]
Pt/SiO_2	2	CO oxidation	>100	/	< 7	Gracia et al. [28]
$Pt/CeO_x/Al_2O_3$	0.4	CO oxidation	50	/	0.29	Mergler et al. [25]
$Pt/MnO_x/SiO_2$	5	CO oxidation	50	/	0. 19	Mergler et al. [25]
$Pt/CoO_x/SiO_2$	5	CO oxidation	0	/	0.33	Mergler et al. [25]
Pt/TiO_2	1	CO oxidation	27	< 6.84	< 0.38	Bamwenda et al. [29]
Pt/TiO_2	0.5	CO oxidation	27	< 0.86	< 0.92	Bamwenda et al. [29]
$K\text{-}Pt/Al_2O_3$	2	PROX	80	24.4	3.3	Minemura et al. [30]
$M\text{-}Pt/Al_2O_3$*	2	CO oxidation	100	/	< 4	Minemura et al. [31]
Pt_3Sn/C	~ 16.6	PROX	80	/	15	Schubert et al. [32]
Pt_1/Fe_2O_3	0.029	CO oxidation	140	205.2	15	Yang Lou et al. [26]
Pt_1/Fe_2O_3	0.029	WGS	140	492.4	26	Yang Lou et al. [26]
Pt_1/Fe_2O_3	0.17	CO oxidation	27	43.5	13.6	Botao Qiao et al. [33]
Pt_1/Fe_2O_3	0.17	PROX	27	67.6	21.2	Botao Qiao et al. [33]
Pt_1/Fe_2O_3	0.17	PROX	80	99.2	31.1	Botao Qiao et al. [33]
Pt/FeO_x	1.5	CO oxidation	27	46.8	15.1	Liu et al. [27]
Pt_x/Fe_2O_3	2.5	CO oxidation	27	17.7	8.01	Botao Qiao et al. [33]
Pt_x/Fe_2O_3	2.5	PROX	27	20.3	9.15	Botao Qiao et al. [33]
Pt_x/Fe_2O_3	2.5	PROX	80	35.8	16.2	Botao Qiao et al. [33]
Pt_1/ZnO	0.034	CO oxidation	140	69.4	5.3	Yang Lou et al. [26]
Pt_1/ZnO	0.034	WGS	140	502.9	44.7	Yang Lou et al. [26]
Pt/CeO_2	0.3	CO oxidation	40	55.16	2.16^a & 4.69^b	Liu et al. [23]
Pt/CeO_2	0.5	CO oxidation	40	53.50	3.01^a & 8.38^b	Liu et al. [23]
Pt/CeO_2	1.0	CO oxidation	40	4.869	3.14^a & 11.93^b	Liu et al. [23]
Pt/CeO_2	2.0	CO oxidation	40	4.553	4.52^a & 19.9^b	Liu et al. [23]
Pt/CeO_2	5.0	CO oxidation	40	2.589	6.99^a & 6.077^b	Liu et al. [23]
Pt/CeO_2	10	CO oxidation	40	2.236	7.63^a & 9.94^b	Liu et al. [23]

* (**M**=Li, Na, K, Rb, Cs)
[a] TOF_a
[b] TOF_b
[c] TOF normalized by the number of Au atoms under the assumption of 30% Au dispersion

Methodology 3

3.1 Sorption

Two types of sorption can be classified, termed *physisorption* and *chemisorption*, according to the definition of how molecules adhere to solid surfaces. Physisorption involves a weak non-specific interaction between adsorbate and adsorbent, e.g., van der Waals forces. On the contrary, chemisorption requires the formation of a chemical bond that makes it a strong specific interaction.

3.1.1 Nitrogen physisorption

Heterogeneous catalysts are commonly used as a powder with a high surface area as the accessible area for reactants in the gas phase is crucial for catalytic performance. The Specific Surface Area (SSA) determines the space to disperse metal particles, which can be obtained from *physisorption* of N_2. The adsorption isotherm reflects the surface coverage changes of N_2 gas molecules with equilibrium pressure, generally at 77K of N_2. In order to obtain SSA from isotherm, Braunauer, Emmett, and Teller (BET) theory is applied. They have generalized the Langmuir isotherm assumptions [1], and take multilayer adsorption into consideration. Further assumptions are made in the following [6]:

- A constant adsorption energy within the first layer.
- The molar heat of condensation is equivalent to the adsorption energy for the rest of layers except the first layer.
- Infinite number of layers are considered when the pressure P equals the saturation pressure P_0.

1: · Only one monolayer formed between gas and solid surface
· An uniform adsorbent surface with identical adsorption sites
· No adsorbate-adsorbate interaction

An example of N_2 adsorption-desorption isotherms for Pt/alumina is shown in Figure 3.1. N_2 molecules start to adsorb at relatively low pressure at Position 1. After a monolayer is formed at Position 2, multilayer adsorption follows. From Position 3 to 4, capillary condensation occurs at a critical thickness, where multiplayer adsorption from vapor phase turn into a condensed liquid phase. This transition happens before the saturation pressure (P_0) due to an increased effect of van der Waals forces inside mesopores. Moreover, Position 5 and 6 correspond to a desorption process. The adsorption-desorption isotherms are classified and this type of hysteresis loop belongs to the H1 type, which describes a material

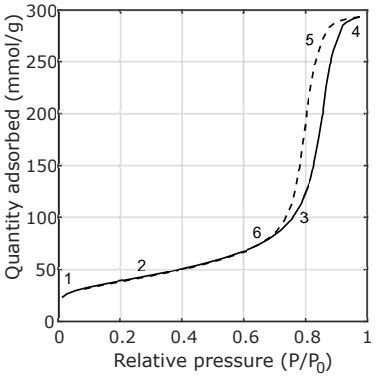

Figure 3.1: N_2 adsorption (solid line) and desorption (dash line) isotherms of Pt/alumina.

with a well-defined cylindrical pores [35].
Afterward, the SSA can be calculated from below, in m^2/g:

$$\mathrm{SSA} = \frac{V_m \sigma N_A}{m V_{N_2}} \tag{3.1}$$

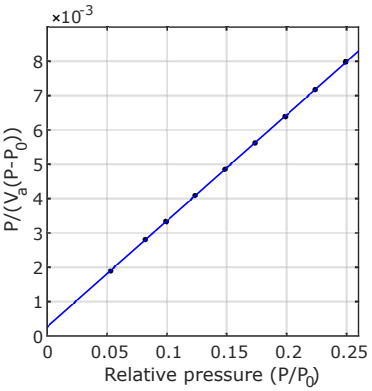

Figure 3.2: BET plot of Pt/alumina.

where σ is the occupied area of a single N_2 molecule on the adsorbent, N_A, the Avogadro constant, m the mass of adsorbent, and V_{N_2} the N_2 gas molar volume at Standard Temperature and Pressure (STP). V_m is the adsorbed gas quantity required to form a monolayer, which can be determined from BET equation as below:

$$\frac{P}{V_a(P_0 - P)} = \frac{1}{cV_m} + \frac{c-1}{cV_m}\frac{P}{P_0} \tag{3.2}$$

where V_a is the total adsorbed gas volume, c a constant only determined by the adsorption heat of first layer, P the pressure and P_0 the saturation pressure. An intuitive BET plot with a defined pressure range is displayed in Figure 3.2, where V_m can be directly retrieved from the slope or intercept of the regression line.

3.1.2 Chemisorption

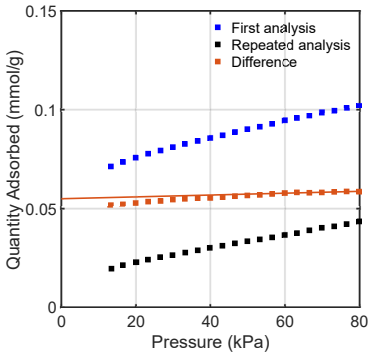

Figure 3.3: CO adsorption isotherms at 35 °C for Pt/alumina. Blue squares depict first analysis including physisorption and chemisorption, while the black ones describe physisorption in the repeated analysis. The orange ones suggest the chemisorption after subtracting the repeated analysis from first analysis.

Efficient utilization of active precious metals with a high dispersion is vital to catalytic activity. The metal dispersion, area, and particle size can be determined from *chemisorption* of, e.g., CO; similarly, the monolayer assumption is granted. In contrast to *physisorption*, *chemisorption* involves electrons being shared between the adsorbate and adsorbent. This is considered as an irreversible process compared to a reversible *physisorption*. Owing to different characteristics of techniques between *physisorption* and *chemisorption*, the latter can be performed by running a second isotherm after the initial adsorption [36]. Vacuum is applied in between to desorb the physisorbed CO. The first isotherm thus contains both *physisorption* and *chemisorption*, while the second isotherm only includes *physisorption*. An example of CO adsorption isotherms for Pt/alumina is displayed in Figure 3.3. The CO *chemisorption* is indicated by the orange squares, and the plateau part (the last 8 points) is used for linear regression. The quantity of chemisorbed CO monolayer per gram catalyst (Q_{CO}, mol/g) at STP, can be obtained from the intercept of linear regression in the example. The corresponding monolayer volume (V_m) in cm^3/g can, of course, be derived from

$$V_m = Q_{CO} V_{CO} \tag{3.3}$$

where V_{CO} is CO molar volume at STP in cm^3/mol. The metal dispersion (D_{metal}) is used to depict the fraction of surface metal sites (that are accessible to CO) over total metal sites. This can be

expressed in:

$$D_{\text{metal}} = \frac{Q_{\text{CO}} M_{\text{metal}} F_s}{W_{\text{metal}}} 100\% \tag{3.4}$$

where M_{metal} is the molar mass of metal in g/mol, W_{metal}, the weight percentage of active metal over sample, and F_s, stoichiometric factor. F_s describes the number of active metal atoms absorbed by one CO molecule, which can be determined from infrared spectroscopy. The active metal area, A_{metal}, that can be accessed by probing molecules, in $\text{cm}^2/(\text{g of sample})$ can be further formulated:

$$A_{\text{metal}} = Q_{\text{CO}} F_s a_s N_A \tag{3.5}$$

where a_s is cross-sectional area of Pt, which is 0.08 nm^2. An additional parameter, particle diameter (d_{metal}), can be evaluated with a certain geometry, here, hemispheres

$$d_{\text{metal}} = \frac{6 \cdot W_{\text{metal}}}{A_{\text{metal}} \rho_{\text{metal}}} \tag{3.6}$$

where ρ_{metal} is the density of pure metal.

3.2 X-ray diffraction

The diffraction pattern originates from the intensity distribution of an optical wave when it is transmitted through an aperture. It comes from the interference of diffracted light, and the maximum intensity can be obtained at a specific angle, named *Bragg angle* θ. This is as a result of constructive interference when the difference of optical path equals to a multiple of the incident wavelength (λ). Thus, Bragg's law can be expressed as:

$$n\lambda = 2d \sin\theta \tag{3.7}$$

where n represents integer, and d is the interplanar spacing. This phenomenon could also happen when X-rays interact with atomic planes inside crystalline structures, termed X-ray diffraction (XRD), and its scheme is presented in Figure 3.4. The mean crystalline size, τ, can be further calculated from the Scherrer equation:

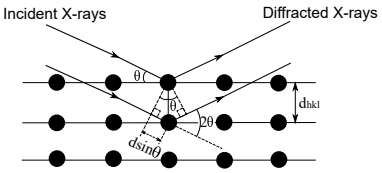

Figure 3.4: Scheme of Bragg's law.

$$\tau = \frac{K\lambda}{\beta \cos\theta} \tag{3.8}$$

where λ is X-ray wavelength (1.54 Å for Cu-Kα), β, the peak broadening of half-maximum intensity at 2θ, in radians, and K, a dimensionless shape factor. The Scherrer equation assumes a perfect crystallinity without any instrumental broadening; however, any crystalline defects, e.g., vacancies, dislocation, or substitution, could cause extra broadening. Small particles thus produce a

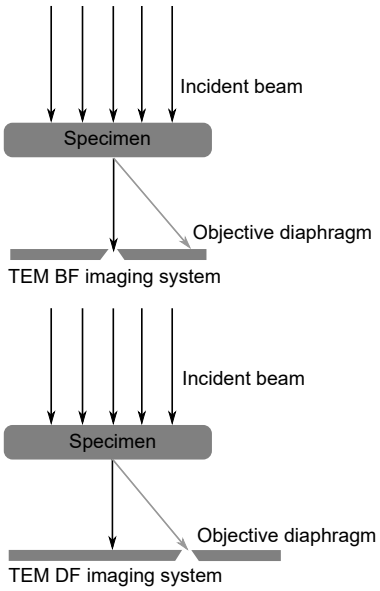

Figure 3.5: Simplified TEM scheme.

2: the number of electrons (or charge) per unit area per unit time

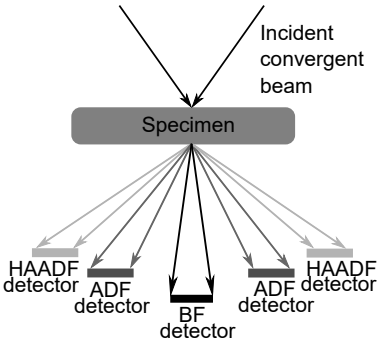

Figure 3.6: Simplified STEM scheme.

broader linewidth in the frequency domain as compared to large particles.

3.3 Transmission electron microscopy with energy-dispersive X-ray spectroscopy

Transmission Electron Microscopy (TEM) is one of the most intuitive and versatile tools to directly observe the shape and size of nanoparticles, their morphology, and crystallographic information. Moreover, chemical compositions can be revealed by Energy-Dispersive X-ray Spectroscopy (EDX). A transmission electron microscope consists of three main parts: the illumination system, the lens, and the image system [37]. FEI Tecnai T20 and Titan 80-300 equipments have employed with different illumination systems, LaB_6 filament at 200 kV and field emission gun at 300 kV, respectively. A field emission gun exhibits a higher brightness [2] and a better vacuum compared to a LaB_6 filament. TEM is not only for TEM imaging, it would also work for Selected-Area Diffraction (SAD), Scanning Transmission Electron Microscopy (STEM), and Electron Energy Loss Spectroscopy (EELS). We will focus on the introduction of TEM imaging and STEM imaging with Bright-Field (BF) and Dark-Field (DF) images. BF and DF images can be distinguished by selecting transmitted or scattered electrons after interacting with the specimen as shown in Figure 3.5. This is achieved by using apertures in TEM mode while applying different detectors in STEM mode. TEM imaging applies a parallel electron beam on the specimen, while STEM imaging utilises a convergent electron beam. Extra detectors are used for different locations: BF detector for the beam with an angle less than 10 mrad, Annular Dark-Field (ADF) detector for a larger angle between 10 to 50 mrad, and High-Angle Annular Dark-Field (HAADF) detector for the angles larger than 50 mrad as displayed in Figure 3.6. An example of TEM and STEM micrographs are presented in Figure 3.7. Figure 3.7 shows a TEM BF image in (a) and a STEM-HAADF image in (b). In TEM BF mode, the image contrast mainly comes from mass-thickness contrast. A thicker sample or heavy element region will scatter more electrons and less electron transmitted, thus giving darker areas of an image. Other contrasts, including diffraction contrast and phase contrast, could also contribute to a crystalline structure. Diffraction contrast is achieved by using objective aperture to filter out the transmitted electrons from scattered ones for a BF image. Phase contrast is a result of the interaction between scattered electrons and transmitted electrons [37]. The mass-thickness contrast primarily contributes to a STEM-HAADF image, where the incoherent elastic scattering is detected and strongly affected by atomic number. Therefore,

a higher atomic number and a thicker sample will allow more elastic scattering, and this will cause a brighter area instead in STEM-HAADF. STEM mode presents a generally better contrast and less noisy image without lens for imaging compared to TEM mode.

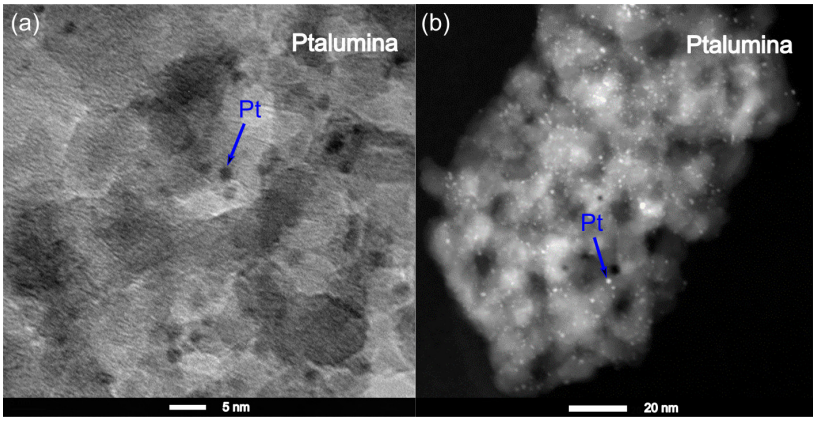

Figure 3.7: TEM (a) and STEM (b) image of Pt/alumina.

3.4 *In situ* and *Operando* catalyst characterization

3.4.1 Infrared spectroscopy

The wavelength of infrared light spanning from 0.8 µm to 1000 µm (14000 cm^{-1} to 10 cm^{-1}) covers near-IR (0.8–2.5 µm), mid-infrared (2.5–25 µm) and far-infrared (25–100 µm). We will focus on the utilization of mid-infrared to excite electrons between vibrational energy levels and associated rotational-vibrational transitions, thus the vibrational spectra of molecules are studied. However, this requires the molecules being IR active, which means molecules with permanent dipole moment or an induced dipole moment variation as it vibrates. So vibrational spectroscopy can't be able to observe for homonuclear molecules, e.g., nitrogen and oxygen, since they have neither permanent dipole moment nor induced dipole moment as the molecules vibrate. Diatomic molecular vibration can be described classically by Hook's law, then the oscillation frequency, w_e, can be expressed in cm^{-1}:

$$w_e = \frac{1}{2\pi c}\sqrt{\frac{k}{\mu}} \tag{3.9}$$

where k is the spring constant, c, the velocity of light, and μ, the reduced mass. The vibrational energy can be obtained considering a simple harmonic oscillatior by solving Schrödingar equation, in

cm^{-1}:

$$E_v = (v + \frac{1}{2})w_e \quad (v = 0, 1, 2, ...) \tag{3.10}$$

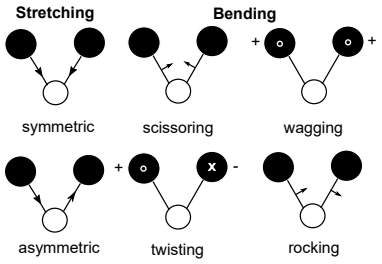

Figure 3.8: Fundamental vibration modes.

where v is called vibrational quantum number. In this case, the emission frequency equals to w_e with the selection rule of $\triangle v = \pm 1$. Whereas, a more complete expression close to the reality would be:

$$E_v = (v + \tfrac{1}{2})w_e - \underbrace{(v + \frac{1}{2})^2 w_e \chi_e}_{\text{anharmonicity}} + \underbrace{B_e J(J+1)}_{\text{rigid rotator}} - \underbrace{D_e J^2 (J+1)^2}_{\text{centrifugal distortion}} - \underbrace{\alpha_e (v + \frac{1}{2}) J(J+1)}_{\text{rovibration interaction}} \tag{3.11}$$

where χ_e is an anharmonicity constant when taking the bond stretch into consideration, and selection rules turn out to be $\triangle v = \pm 1, \pm 2$, etc., B_e, the rotation constant after considering a rigid rotational vibration. D_e, the additional centrifugal distortion constant under Born-Oppenheimer approximation, where vibrations and rotations are assumed to be independent. α_e is rovibrational coupling constant with selection rule of $\triangle v = \pm 1, \pm 2$, etc. $\triangle J = \pm 1$. The number of fundamental vibrations can be calculated for polyatomic molecules. If the molecules are non-linear, the vibrations will be 3N-6. Whereas it will be 3N-5 for linear molecules, including N-1 for stretching mode and 2N-4 for bending mode, and 2N-5 for non-linear ones [38]. The fundamental vibration modes are shown in Figure 3.8.

Two operation modes can be performed in Infrared Spectroscopy (IR); one is transmission, the other is in reflectance mode. Diffuse reflectance happens when the incident infrared beam is exposed on a rough sample surface, then reflects in all directions rather than a specular direction. *In situ* DRIFTS is performed for probing adsorbed molecular species on the sample surface. The absorbance, A, can be expressed in terms of diffuse reflectance mode using Beer-Lambert law in Eq. 3.16. In DRIFTS, the infrared spectra are

$$I_R = I_0 - I_T \tag{3.12}$$
$$I_T = I_0 \cdot e^{-\mu x} \tag{3.13}$$
$$A = \mu x \tag{3.14}$$
$$R = \frac{I_0}{I_R} \tag{3.15}$$
$$A = \log_{10}(\frac{1}{R}) \tag{3.16}$$

where I_0 is the intensity of incident infrared light, I_T, the intensity of transmitted light, I_R, the intensity of diffuse reflectance, μ, absorption coefficient in cm^{-1}, and x, the absorption depth

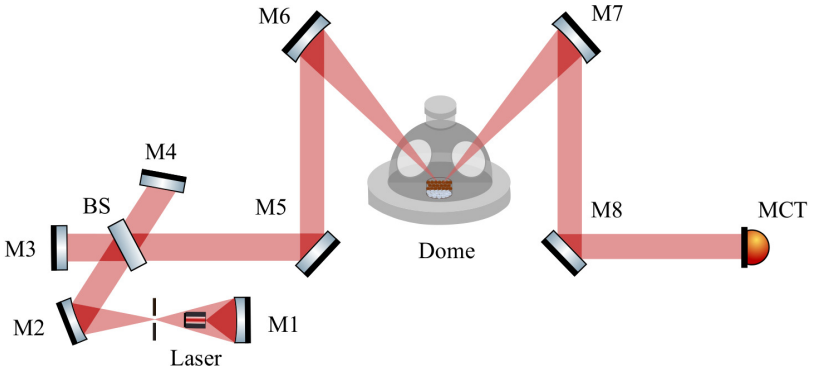

Figure 3.9: A schematic setup of DRIFTS, where M abbreviates for mirror with a movable mirror of M4, BS representing for Beam Splitter, and MCT denoting a Mercury-Cadmium-Telluride detector.

measured by a Michelson interferometer as shown in Figure 3.9, where a movable mirror can scan for $\triangle/2$ with a path difference of $\triangle$. The path difference will generate an interferogram with all the

spectral lines recorded at the same time. A vibrational spectrum of adsorbates can be obtained after subtracting a background taken at the same experimental condition but in a pure Ar flow. An IR spectrum of CO adsorbed on Pt/alumina catalyst is presented in Figure 3.10. The vibrational band of gaseous CO is centered at 2150 cm^{-1} with P and R branches arising from $\triangle J = \pm 1$, while the rest of the peaks can be assigned to different CO adsorption configurations on various size of Pt sites [39]. As for adsorbed CO, the increased π-backbonding from large Pt particles to CO molecules gives the shift between the absorption peaks for linear and bridge bond CO.

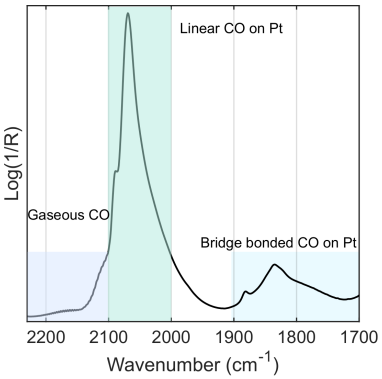

Figure 3.10: Infrared spectrum of CO adsorbed on Pt/alumina.

3.4.2 X-ray absorption spectroscopy

XAS unravels the connection between structure and catalytic activity even during reaction conditions. This provides us a deeper insight into the function of catalysts under reaction conditions. XAS could be detected in two operation modes, *transmission* and *fluorescence*. As shown in Figure 3.11, when X-rays incident on samples, multiple events will occur. The transmission will be primarily detected in the same direction as the incident X-rays, accompanied by a photoejected electron. This is followed by the generation of a core-hole[3]. When filling in the core-holes by higher energy level electrons, the energy could be released in a form of an emitted photon, named *fluorescence*, or the energy can be transferred to another ejected electron, called *Auger electron*. The *fluorescence* yield can thus be decreased by the production of *Auger electrons* and can be enhanced with a higher atomic number. The radiation of *fluorescence* and *Auger electrons* proceeds from all directions. Other elastic and inelastic scattering events, diffracted by tightly or loosely bound electrons, could also occur. The transmitted intensity, I, can be expressed by *Beer-Lambert law*:

$$I(\lambda) = I_0(\lambda) \exp(-\mu x) \tag{3.17}$$

where I_0 is the intensity of incident X-rays with a wavelength of λ, x, the sample thickness, and μ, the absorption coefficient of the sample, in cm^{-1}. A more convenient expression is in mass absorption coefficient, μ/ρ in cm^2/g. This is a wavelength-dependent coefficient, which decreases with reduced wavelength within X-ray range. However, it increases dramatically at the energies which could remove an inner-shell electron to continuum state, and generates an *absorption edge*. The absorption coefficient can further determine the intensity of *fluorescence* signal, I_f, and is proportional to I_f/I_0. Other characteristic emissions from the rest of the elements in the sample will give a background in *fluorescence* signal, which can be filtered out by selecting a detector with a proper

3: the vacancy left after liberating the core electron of an atom

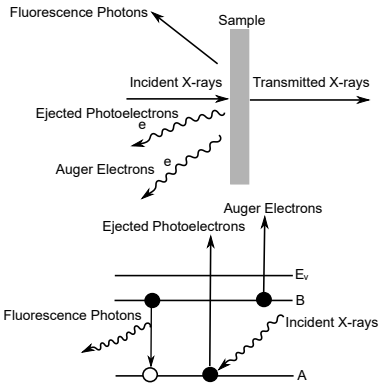

Figure 3.11: A schematic representation of multiple events after X-ray absorption.

wavelength range.
XAS is an absorption spectroscopy technique using X-rays, with wavelengths around 0.1–50 Å. X-rays will interact with the electrons of an atom and have enough energy to kick out an inner shell electron. This energy can be described as threshold energy of *absorption edge*, E_0. XAS can be divided into several regions according to the relationship between the incident energy, E, and the threshold energy, E_0 [40].

- The *pre-edge* region is when $E < E_0$, pre-peaks are created by the transitions of core electrons to partially filled or unoccupied bound states
- The *edge* is induced when $E \approx E_0$ from the electronic transitions to empty energy levels and/or continuum states
- The X-ray Absorption Fine Structure (XAFS) part is introduced when $E > E_0$, and two regions of X-ray Absorption Near Edge Structure (XANES) and EXAFS are included. XANES is generally located within ±10 eV around E_0, while EXAFS normally starts from 50 eV higher than E_0 [40]. The photoelectron goes out with a kinetic energy, E_k=$E - E_0$, and the wavelength of outgoing photoelectron can be expressed in $\lambda_e = \frac{h}{\sqrt{2m_e(E-E_0)}}$, where m_e is the mass of an electron, and h the Planck constant.

The reason for XAFS oscillation is that the electromagnetic wave of the ejected photoelectron will interfere with the wave from backscattered photoelectrons in the neighborhood constructively or destructively. The constructive interference will increase the electron density, and a higher absorption probability can be obtained. Therefore, a transition from constructive to destructive interference will reflect a maximum to minimum absorption. Whereas no XAFS can be observed for monoatomic gas. As displayed in Figure 3.12 panel (a), different regions are marked in a XAS spectrum of liberating electrons from the 2p orbital of the Pt LIII edge. Different regions could provide various information. The *pre-edge* could deliver some information about coordination geometry, while the

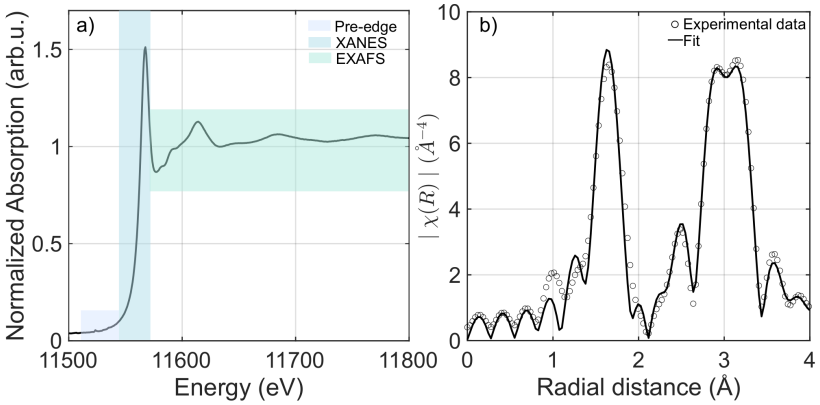

Figure 3.12: XAS spectra of PtO_2 powder sample in *fluorescence* mode (a) and its fourier transformation with a fit (b).

absorption edge in XANES, also called *whiteline*, indicates a chemical state. The electrons of the element with a higher oxidation state tolerate more attractive coulombic forces from nuclei than a lower oxidation state. One needs to provide more energy to liberate the electrons, and an increased absorption probability is due to additional unoccupied energy levels. Thus, a shift to higher energy for E_0 and a stronger Whiteline Intensity (WLI) would be expected.

EXAFS is sensitive to local structure about the distance to near neighbors and coordination number of the neighboring atoms. The oscillation in EXAFS region, $\chi(k)$, can be further analysed quantitatively by EXAFS equation:

$$\chi(k) = \sum_j A_j(k)\sin[2kR_j + \phi_j(k)] \tag{3.18}$$

where $A_j(k)$ is the backscattering amplitude from atoms in the jth shell, R_j, the distance between the absorbing atom and atoms in the jth shell, and $\phi_j(k)$, the phase shift induced by coulomb interaction between absorbing atom and atoms in the jth shell. k, the wavenumber can be derived from $\frac{2\pi}{\lambda_e}$. Moreover, this equation can be expanded with consideration of multiple scattering.

$$\chi(k) = \sum_j \frac{N_j \cdot S_0^2(k)}{k \cdot R_j} \mid f_{\text{eff}}(k)_j \mid \cdot \exp(-2k^2\sigma_j^2) \cdot \exp[\frac{-2R_j}{\wedge(k)}]\sin[2kR_j + \phi_j(k)] \tag{3.19}$$

where N_j represents the number of backscatters in jth shell, $S_0^2(k)$ describes the relaxation effect for the absorbing atom after the removal of electrons, $f_{\text{eff}}(k)_j$, the effective amplitude for single scattering path. σ_j, the Debye-Waller factor depicting thermal disorder, and $\wedge(k)$, the mean free path of photoelectrons. EXAFS analysis is performed by fitting background-subtracted experimental data into theoretical scattering pathways. The theoretical paths are built based on the knowledge about the structure of catalysts, and several parameters in Eq. 3.19 can be estimated from *ab initio* theoretical calculations, $f_{\text{eff}}(k)_j$, $\phi_j(k)$, $\wedge(k)$, and R_j. Fine-tuning R_j, N_j and σ_j can minimize the difference between experimental data and theory. S_0^2 is normally obtained from a standard reference sample employing the same experimental setup, and this value is theoretically around 0.7- 1.1 [40]. However, it could be higher in transmission mode due to a strong fluorescence signal or lower due to self-absorption in fluorescence mode. Also, experimental conditions will play a role. The contributions from a heavy and a light element can be easily distinguished after fourier transform. An fourier transformed EXAFS spectrum of PtO_2 powder in radial distribution (without phase correction) is displayed in Figure 3.12 panel (b). The Pt-O and Pt-Pt contribute at different radial distances. The Pt-O radial distance is located at 1–2 Å, while the Pt-Pt scattering paths contribute at around 3 Å.

3.5 Catalyst evaluation in a fixed-bed reactor

3.5.1 Fixed-bed reactor setup

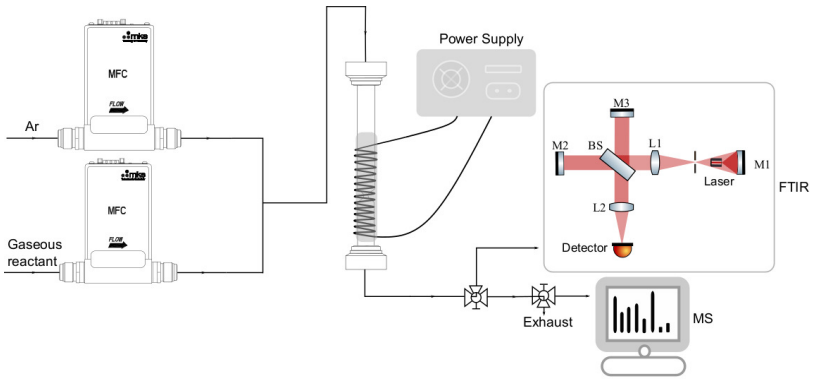

Figure 3.13: A schematic presentation of a flow reactor setup.

A fixed-bed flow reactor was utilized, and its setup schematically is presented in Figure 3.13. The gas flow is controlled by several Mass Flow Controllers (MFCs), and the total flow is balanced by Argon throughout all the experiments. The reactor is a 33 cm long quartz tube placed vertically with an inner diameter of 4 mm and an outer diameter of 6 mm. A metal coil was spiraled around the reactor for resistive heating and covered with a quartz wool layer outside, while the rest of the tubing is twisted by the heating band and wrapped by insulators to avoid condensation. The sample was primarily sieved to 40–80 µm, then mixed with crushed cordierite with a particle size of 300–355 µm to mitigate the pressure drop. The mixture with sample and cordierite (1:30) was loaded into the reactor to even out the heat from the exothermic reaction. Two thermocouples were used to regulate the inlet gas temperature and monitor the temperature of the sample bed, which can be heated by the reaction. The regulated one is placed 1-2 mm above the mixture, while the other is inserted inside the sample. Eventually, the effluent gas is analyzed by a mass spectrometer or Fourier Transformed Infrared (FTIR), which has been described above.

3.5.2 Mass spectrometry

Mass Spectrometry (MS) has been widely applied to identify and quantify the real-time gas composition. This is achieved by the ionisation of various gases, and charged gaseous ions can be subsequently separated according to their mass-to-charge ratio (m/z). The relative abundances of each type of ions can be recorded. A typical mass spectrometer consists of three main parts: an ion source, analyzer, and detector system. A higher vacuum environment is also required before introducing an ion source. An electron ionization with an electron beam is employed to produce

an ion source. Later, all these ions can be resolved by applying a magnetic field, then the ions with the same *m/z* will deflect in the same direction. In the end, the sorted ions will reach the detector and produce an abundance spectrum. By comparing the spectra with databases, one can figure out the composition. Sometimes fragmentation is useful to distinguish the molecules with the same *m/z*, e.g., carbon monoxide and nitrogen. Their main characteristic peak is presented at a *m/z* of 28, but nitrogen will give a signal at 14 (*m/z*), but relatively lower than the one at 28 (*m/z*).

Results and discussion 4

Supported Pt catalysts have been used effectively for CO oxidation in many aspects, while low-temperature CO oxidation is concerned due to the upcoming more sever vehicles emission legislation. Thus, Pt nanoparticle catalysts with reducible and non-reducible supports are selected to study. We first look at the physicochemical properties in Paper I. Kinetics, and the possible mechanisms are proposed together with DFT calculations in Paper I&II. *Operando* spectroscopy bridges the view of catalysts from the macroscopic to the microscopic level. The local structure combined with active species changes during CO oxidation is further investigated in Paper I for understanding how the dynamics are modified for small Pt particles by different support materials during the catalytic extinction of CO oxidation.

4.1 Physicochemical properties of catalysts

The catalysts of 2 wt% Pt/alumina and 1 wt% Pt/ceria are used to investigate the catalytic performance discrepancy for reducible and non-reducible supports. A summary of physicochemical properties of 2 wt% Pt/alumina and 1 wt% Pt/ceria is displayed in Table 4.1. The SSA of Pt/alumina and Pt/ceria is measured by nitrogen physisorption, to be 131 and 140 m^2/g, respectively. This is mainly represented by the surface area of the support and sufficiently large enough to provide a high Pt dispersion. The specific Pt area for Pt/ceria is 1.92 m^2/g, lower than that of Pt/alumina, but a higher Pt dispersion is achieved. These results likely signify a more homogeneous Pt size distribution over ceria compared to alumina. Moreover, the Pt particle size is measured by two methods: CO chemisorption and STEM micrographs. In general, the Pt particle size for Pt/ceria is smaller than those of Pt/alumina. However, CO chemisorption gives a larger estimation of Pt particle size compared to the results from STEM micrographs. The discrepancy may come from a limited number of analysed Pt particles and a possible reduction induced by the electron beam in STEM. Contrary, CO chemisorption gives an average size of Pt particles based on a simple assumption of hemispherical particle shape. The size of the support material is calculated from XRD measurements by employing Debye-Sherrer equation, to be 6 nm and 8 nm for ceria and alumina support, respectively. The Pt/ceria and Pt/alumina

Table 4.1: Specific Surface Area (SSA) of catalysts and metal (SSA_{Pt}), Pt loading (X_{Pt}), metal dispersion (D_{Pt}), Pt particle size (d_{Pt}), and support particle size ($d_{support}$) for Pt/ceria and Pt/alumina.

properties	Pt/ceria	Pt/alumina
SSA (m^2/g)	131	140
SSA_{Pt} (m^2/g)	1.92	2.65
X_{Pt} (wt%)	1.06	1.91
D_{Pt} (%)	78	54
d^a_{pt} (nm)	1.45	2.11
d^b_{pt} (nm)	1 ± 0.22	1.29 ± 0.43
$d_{support}$ (nm)	approx. 6	approx. 8

[a] Obtained from CO chemisorption
[b] Analysed from STEM images

catalysts are further imaged by TEM and STEM in Figure 4.1.

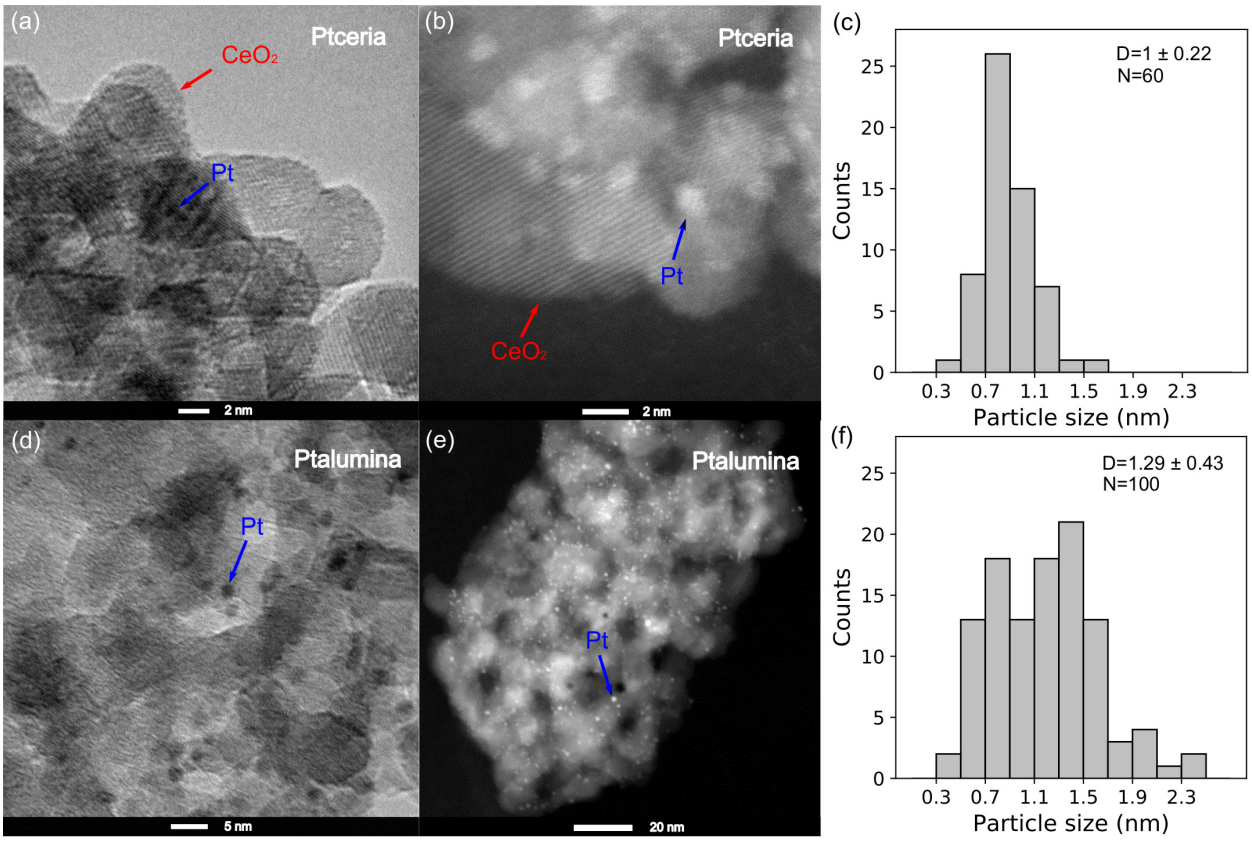

Figure 4.1: HRTEM (panel a and d) and STEM (panel c and e) micrographs of Pt/ceria and Pt/alumina catalysts. The corresponding Pt particle size distributions in panel c and f.

Pt/ceria exhibits a mean Pt particle size of 1 nm within a size range of 0.3-1.7 nm, while the majority of Pt particles for Pt/alumina is less than 2 nm with a wider range of 0.3-2.5 nm. Not only the size of the Pt particles is studied by TEM but also the size of crystallites of the support materials. The crystallite size is 6 and 10 nm for the ceria and alumina support, respectively. These are in line with the results from the XRD analysis, which assumes a perfect crystallinity and no instrumental broadening.

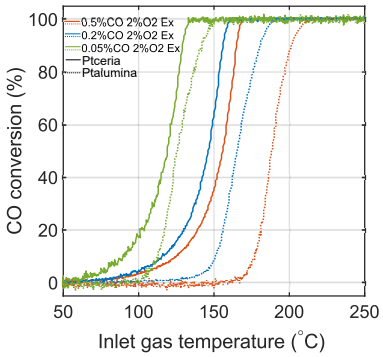

Figure 4.2: Extinction profiles for CO oxidation over Pt/ceria and Pt/alumina catalysts under 0.5% CO (orange), 0.2% CO (blue), 0.05% CO (green) and 2% O_2.

4.2 Kinetics

4.2.1 Behaviour in extinction

The extinction profiles for CO oxidation over 2 wt% Pt/alumina and 1 wt% Pt/ceria are displayed in Figure 4.2. One can clearly observe a shift to a higher temperature with elevated CO concentration for the extinction profiles for both catalysts. This is, of course, due to more CO self-poisoning, but to different extents for the Pt/ceria and the Pt/alumina catalyst. The CO conversion for

Pt/ceria drops at 170, 160 and 135 °C when the CO concentration changes from 0.5, 0.2 and 0.05% CO with 2% O_2. A larger deviation in temperature, from 215 to 150 °C, has been observed for Pt/alumina when decreasing the CO concentration from 0.5% to 0.05%. These results are in agreement with previous studies [41]. Pt/ceria is more active than Pt/alumina for CO oxidation under lean conditions with a low specific Pt area mentioned above. The superior activity becomes more evident in the low-temperature regime with characteristic conversion profiles that are more smooth for Pt/ceria than an abrupt change for Pt/alumina. This difference reflects complementary reaction paths could work in the low-temperature region for Pt/ceria, which has been explored thereafter.

4.2.2 Reaction order reflecting possible reaction mechanisms

The reaction order experiments were carried out in a flow reactor as described above, and the reaction rate is controlled by kinetics. The obtained O_2 and CO reaction order for Pt/ceria is 0.10 and -0.18 respectively, as shown in Figure 4.3a. This corroborates a Mars-van Krevelen mechanism for Pt/ceria with Eq. 2.21 as a RDS. In **Paper II**, a model with Pt_{34} (34 Pt atoms) supported on CeO_2 (111) is used for kinetic Monte Carlo simulations with kinetic parameters evaluated from Density Functional Theory (DFT) calculations. The reaction barrier, E_a, is calculated from a Brønsted-Evans-Polanyi relation depending on CO and O adsorption energy. Further, a rod-model with 32 Pt atoms on CeO_2 (111) is used to obtain the barriers for CO oxidation at the interface. The normal reaction pathways include CO adsorption, desorption and diffusion, and O_2 dissociative adsorption and further diffusion. CO_2 is formed from the reaction between adsorbed CO and O. The interface reaction pathways are considered via the reaction between adsorbed CO and an oxygen atom on the surface of CeO_2(111). This oxygen vacancy site can be refilled by the adsorption of molecular oxygen which subsequently reacts with adsorbed CO to produce CO_2. The result from the simulations show the light-off temperature is determined by the interface reaction which is in line with the experimental results. On the contrary, the reaction order for Pt/alumina is 0.62 for O_2 and -1.09 for CO in Figure Figure 4.3b, which resembles closely to a Langmuir-Hinshelwood mechanism with oxygen dissociation.

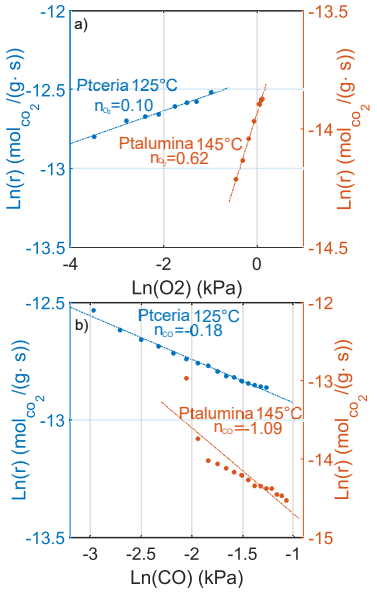

Figure 4.3: O_2 (a) and CO (b) reaction order over Pt/ceria and Pt/alumina catalysts.

4.3 *Operando* spectroscopy

4.3.1 Surface species evolution

A steady-state catalytic CO oxidation extinction is focused to analyse the surface species by *operando* DRIFTS. In Figure 4.4 panel a and c shows a $\tilde{\nu}_{gas}^{CO_2}$ spectral region over Pt/ceria and Pt/alumina catalysts. This reflects the catalytic activity since CO_2 formation is the only product. In panel b and d display a different CO ad-species at a lower wavenumber region. We start with the results for the Pt/ceria catalyst, the intensity of $\tilde{\nu}_{gas}^{CO_2}$ band decreases with lowering temperature. Until 81 °C, the $\tilde{\nu}_{gas}^{CO_2}$ band almost vanishes. Whereas, CO adsorption peak at 2107 cm^{-1}, assignable to $\tilde{\nu}_{lin}^{CO}(Pt^{2+})$ [12], keeps growing upon decreasing temperature although a significant CO_2 production. A shoulder peak at 2078 cm^{-1} assigned to $\tilde{\nu}_{lin}^{CO}(Pt^{\delta+})$ [42] starts to appear at 125 °C as well as two $\tilde{\nu}_{br}^{CO}(Pt)$ bands on larger Pt particles [43] at 1878 cm^{-1} and 1850 cm^{-1} when a minor CO_2 is produced. The presence of this peak reflects the existence of PtO_x clusters, while the single-atom catalyst (SAC) only exhibits a highly symmetric ionic Pt atop absorption peak [44, 45]. Moving to the Pt/alumina catalyst, a similarly continuous decreasing trend of $\tilde{\nu}_{gas}^{CO_2}$ band is observed upon lowering temperature. But a qualitatively different behaviour is noticed for CO ad-species. The $\tilde{\nu}_{gas}^{CO_2}$ band drops after reaching 116 °C where $\tilde{\nu}_{lin}^{CO}(Pt^0)$ band at 2069 cm^{-1} [39, 46] significantly grows. The peaks at lower wavenumbers: 1881 cm^{-1} and 1835 cm^{-1} corresponding to $\tilde{\nu}_{br}^{CO}(Pt)$ bands [47, 48] show up at 108 °C where CO_2 formation completely disappears. This is the temperature

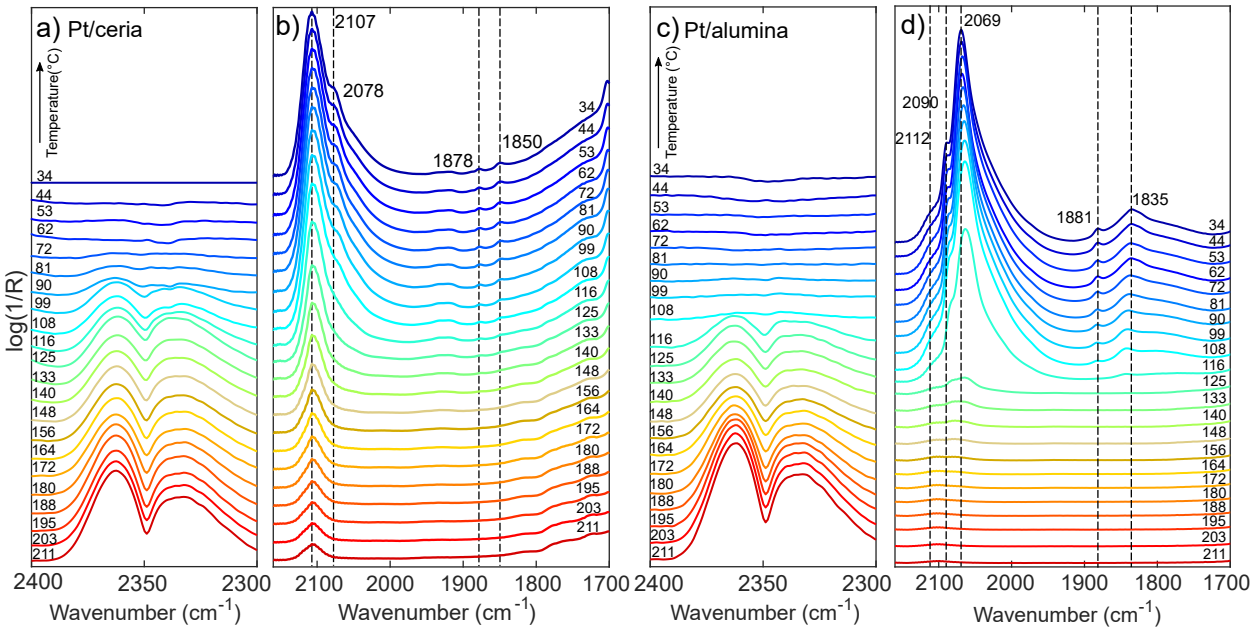

Figure 4.4: CO_2 production and CO adsorption over Pt/ceria (panel a and b) and Pt/alumina (panel c and d) during extinction of CO oxidation with 0.2% CO and 1% O_2.

when the Pt sites get poisoned by CO with a declined catalytic activity, which agrees with the behaviour of extinction profile above. A red-shift of $\tilde{\nu}_{lin}^{CO}(Pt^0)$ is expected during extinction when the oxidised Pt particles are reduced by CO. However, this is not clear after the build-up of $\tilde{\nu}_{lin}^{CO}(Pt^0)$ band. An explanation is that the red-shift is likely cancelled by increasing CO coverage which leads to a blue-shift.

$\tilde{\nu}_{lin}^{CO}$ species is observed to be the most abundant species for both catalysts. However, the characteristic peak for Pt/ceria is $\tilde{\nu}_{lin}^{CO}(Pt^{2+})$ while $\tilde{\nu}_{lin}^{CO}(Pt^0)$ band is detected for Pt/alumina when comparing the CO ad-species between Pt/ceria and Pt/alumina catalysts at low temperatures. This clearly reveals a direct influence from support on the chemical properties of Pt particles and agrees with the observation of smaller Pt particles on ceria than on alumina. The $\tilde{\nu}_{lin}^{CO}(Pt^{2+})$ and $\tilde{\nu}_{lin}^{CO}(Pt^{\delta+})$ bands are the most stable CO ad-species for Pt/ceria and Pt/alumina, respectively. This signifies the most reactive species with CO is the linear CO adsorption on oxidised Pt particles. These oxidised Pt particles are generally due to the interaction between support and small Pt particles.

4.3.2 Local structure evolution

DRIFTS, as a surface-sensitive technique, can be complemented with XAS experiments as a sample-average technique, and a comprehensive understanding of how the support affects the dynamics of the Pt particles by local structure exploration. XANES and EXAFS analysis are introduced in the following discussion here. The steady-state XAS experiments are carried out with a similar gas composition as DRIFTS measurements. In Figure 4.5 panel a and b display the normalised XANES spectra and the fitted k^2-weighted EXAFS spectra for both catalysts during catalytic extinction with as prepared sample, Pt black and PtO_2 as references. As revealed by XANES spectra, there is no observable change in the intensity of Pt L3 edge and as-prepared Pt/ceria exhibits the highest intensity. The origin of the Pt oxidation state is investigated by a consecutive EXAFS analysis. A notable peak as presented in Figure 4.5 panel (b), at about 1.5–2 Å for Pt/ceria, is assignable to Pt-O single scattering path. This represents that the oxidation state mainly comes from the oxygen atoms in the neighborhood. In addition, this peak can be found in PtO_2 reference sample. Therefore, one can clearly observe an oxidised state throughout CO oxidation with lowering temperatures, even at RT. Moving to the Pt/alumina catalyst, the Pt L3 intensity in Figure 4.6 panel a shows a clear drop between 168 and 154 °C. Similarly, as-prepared Pt/alumina stays in an oxidised state. The XANES spectrum at 168 °C closely

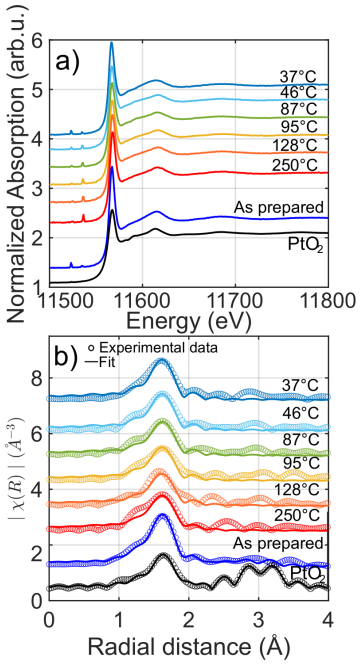

Figure 4.5: XAS spectra (a) and FT K^2-weighted EXAFS spectra (b) over Pt/ceria during CO oxidation from 250 °C to 37 °C.

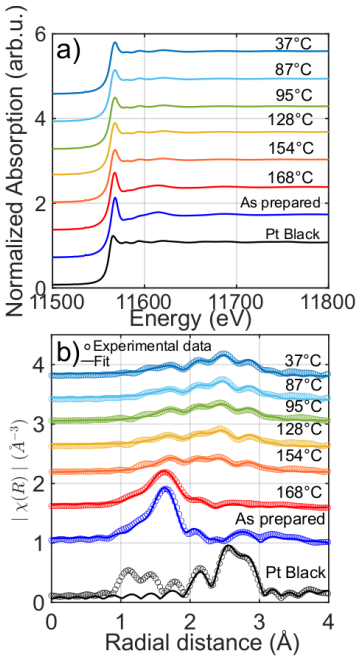

Figure 4.6: XAS spectra (a) and FT K^2-weighted EXAFS spectra (b) over Pt/alumina during CO oxidation from 168 °C to 37 °C.

resembles the spectrum of as prepared catalyst, while the rest of the spectra at lower temperatures is analogous to the one of Pt black sample. Likewise, the EXAFS spectra in panel b exhibits an obvious Pt-O contribution at 168 °C. However, a pronounced peak at 2.5–3 Å, assignable to Pt-Pt single scattering contribution, starts to appear at 154 °C by sacrificing Pt-O contribution.

Combining the results from DRIFTS and XAS experiments, the oxidised Pt state comes from O_2 dissociation on Pt particles during CO oxidation at high temperature. Upon decreasing temperatures, platinum oxide particles get reduced and poisoned by CO molecules preferentially adsorbed on Pt sites. Whereas, a minor Pt-O contribution could also be noticed likely due to these smaller Pt particles get oxidised with the presence of oxygen.

In brief, the difference in the dynamics of Pt particles caused by support interaction leads to a qualitatively different extinction behaviour. Here we emphasise the importance of the combination of *operando* techniques by judging from XAS results alone Pt/ceria catalyst would be assumed to be active at all temperatures. But with the results of infrared spectroscopy, Pt/ceria is apparently CO self-poisoned at low temperatures.

Conclusions and future work

5

The physicochemical characterisation revealed small Pt particles, around 1-2 nm, highly dispersed on ceria and alumina. The Pt/alumina catalyst exhibits a higher specific Pt area but a lower Pt dispersion. In contrast to Pt/alumina, a narrower particle size distribution is realized for the Pt/ceria catalyst which signifies not only small but also uniform Pt particles distributed on the ceria support. CO oxidation over Pt/alumina and Pt/ceria catalyst has been studied by flow reactor for kinetics, *operando* infrared and XAS spectroscopy for the chemistry of Pt particles during catalytic extinction. Kinetic studies presented the extinction profile during CO oxidation for the Pt/ceria catalyst decays slowly rather than a sudden drop in CO conversion for the case of Pt/alumina catalyst. Moreover, a less dependence of extinction temperature on feeding CO concentration is noticed for the Pt/ceria in contrast to the Pt/alumina. These behaviours can be explained by the interaction of small Pt particles with reducible and non-reducible supports, and complementary reaction paths occurring on the interface sites between Pt and ceria. *Operando* DRIFTS showed $\tilde{\nu}_{lin}^{CO}$ as the most abundant species for both catalysts. Nonetheless, the characteristic peak for the Pt/ceria catalyst is $\tilde{\nu}_{lin}^{CO}(Pt^{2+})$, while for the Pt/alumina catalyst is $\tilde{\nu}_{lin}^{CO}(Pt^{0})$. This difference reflects that the chemical properties of the Pt particles are directly influenced by support. This technique combined with XAS further revealed the reason for an oxidised Pt/ceria catalyst throughout the catalytic extinction, even at RT, is mainly due to small Pt particles bind strongly with ceria, as evidenced by an unaltered change of Pt-O bond distance of around 2 Å. Likely, a charge transfer from Pt particles to ceria together with an oxygen reverse spillover from ceria to the vicinity of Pt particles could also contribute to this, however, it is hard to quantify this contribution experimentally. On the contrary, Pt/alumina catalyst only prevails an oxidised state at high temperature due to O_2 dissociation, and adsorbed CO partially removes the oxygen from platinum oxide particles at low temperatures.

Future work will focus on catalytic design with Pt particles on other reducible support materials or stabilizing PtFe alloy nanoparticles for CO oxidation. Of course, exploring the performance between Pt/ceria and Pd/ceria as three-way catalysts will also be highly interesting.

Bibliography

[1] R. M. Heck, R. J. Farrauto, *Applied Catalysis A: General* **2001**, *221*, 443–457.

[2] M. Shelef, R. W. McCabe, *Catalysis Today* **2000**, *62*, 35–50.

[3] T. R. Board, N. R. Council, *The Ongoing Challenge of Managing Carbon Monoxide Pollution in Fairbanks, Alaska*, National Academies Press, **2002**.

[4] P. G. Boulter, *Enviromental traffic management: A review of factors affecting cold-start emissions*, Transport Research Laboratory.

[5] I. Chorkendorff, J. W. Niemantsverdriet, *Concepts of Modern Catalysis and Kinetics* **2003**.

[6] M. Beller, A. Renken, R. A. van Santen, *Focus on Catalysts* **2012**, *2012*, 8.

[7] H. Bönnemann, *Applied Organometallic Chemistry* **2008**, *22*, 412–412.

[8] F. E. Kühn, *Angewandte Chemie International Edition* **2013**, *52*, 2650–2650.

[9] H. S. Gandhi, G. W. Graham, R. W. McCabe, *Journal of Catalysis* **2003**, *216*, 433–442.

[10] X. F. Yang, A. Wang, B. Qiao, J. Li, J. Liu, T. Zhang, *Accounts of Chemical Research* **2013**, *46*, 1740–1748.

[11] K. Liu, A. Wang, T. Zhang, *ACS Catalysis* **2012**, *2*, 1165–1178.

[12] L. Nie, D. Mei, H. Xiong, B. Peng, Z. Ren, X. I. P. Hernandez, A. DeLaRiva, M. Wang, M. H. Engelhard, L. Kovarik, A. K. Datye, Y. Wang, *Science* **2017**, *358*, 1419–1423.

[13] N. K. Soliman, *Journal of Materials Research and Technology* **2019**, *8*, 2395–2407.

[14] A. P. Jia, S. Y. Jiang, J. Q. Lu, M. F. Luo, *Journal of Physical Chemistry C* **2010**, *114*, 21605–21610.

[15] M. Cargnello, V. V. Doan-Nguyen, T. R. Gordon, R. E. Diaz, E. A. Stach, R. J. Gorte, P. Fornasiero, C. B. Murray, *Science* **2013**, *341*, 771–773.

[16] A. D. Allian, K. Takanabe, K. L. Fujdala, X. Hao, T. J. Truex, J. Cai, C. Buda, M. Neurock, E. Iglesia, *Journal of the American Chemical Society* **2011**, *133*, 4498–4517.

[17] M. Kinne, T. Fuhrmann, J. F. Zhu, C. M. Whelan, R. Denecke, H. P. Steinrück, *Journal of Chemical Physics* **2004**, *120*, 7113–7122.

[18] J. Wintterlin, S. Völkening, T. V. Janssens, T. Zambelli, G. Ertl, *Science* **1997**, *278*, 1931–1934.

[19] T. Bunluesin, E. S. Putna, R. J. Gorte, *Catalysis Letters* **1996**, *41*, 1–5.

[20] J. Thank, P. J. Berlowitz, Charles, H. F. Peden, D. W. Goodman, *Journal of Physical Chemistry* **1988**, *92*, 5213–5221.

[21] V. P. Zhdanov, B. Kasemo, *Applied Surface Science* **1994**, *74*, 147–164.

[22] R.H. Julian, *Focus on Catalysts* **(2019)**, *2019*, 7.

[23] H. H. Liu, Y. Wang, A. P. Jia, S. Y. Wang, M. F. Luo, J. Q. Lu, *Applied Surface Science* **2014**, *314*, 725–734.

[24] H. F. Scott, *Elements of chemical reaction engineering*, Prentice Hall, **2016**.

[25] Y. J. Mergler, A. Van Aalst, J. Van Delft, B. E. Nieuwenhuys, *Applied Catalysis B: Environmental* **1996**, *10*, 245–261.

[26] Y. Lou, J. Liu, *Industrial and Engineering Chemistry Research* **2017**, *56*, 6916–6925.

[27] L. Liu, F. Zhou, L. Wang, X. Qi, F. Shi, Y. Deng, *Journal of Catalysis* **2010**, *274*, 1–10.

[28] F. J. Gracia, L. Bollmann, E. E. Wolf, J. T. Miller, A. J. Kropf, *Journal of Catalysis* **2003**, *220*, 382–391.

[29] G. R. Bamwenda, S. Tsubota, T. Nakamura, M. Haruta, *Catalysis Letters* **1997**, *44*, 83–87.

[30] Y. Minemura, S. I. Ito, T. Miyao, S. Naito, K. Tomishige, K. Kunimori, *Chemical Communications* **2005**, 1429–1431.

[31] Y. Minemura, M. Kuriyama, S. ichi I., K. Tomishige, K. Kunimori, *Catalysis Communications* **2006**, *7*, 623–626.

[32] M. M. Schubert, M. J. Kahlich, G. Feldmeyer, M. Hüttner, S. Hackenberg, H. A. Gasteiger, R. J. Behm, *Physical Chemistry Chemical Physics* **2001**, *3*, 1123–1131.

[33] B. Qiao, A. Wang, X. Yang, L. F. Allard, Z. Jiang, Y. Cui, J. Liu, J. Li, T. Zhang, *Nature Chemistry* **2011**, *3*, 634–641.

[34] J. Nilsson, P. A. Carlsson, N. M. Martin, E. C. Adams, G. Agostini, H. Grönbeck, M. Skoglundh, *Journal of Catalysis* **2017**, *356*, 237–245.

[35] F. Ambroz, T. J. Macdonald, V. Martis, I. P. Parkin, *Small Methods* **2018**, *2*, 1800173.

[36] P. A. Webb, *MIC Technical Publications* **2003**, *13*, 1–4.

[37] D. B. Williams, C. B. Carter, *Transmission Electron Microscopy*, Springer US, **2009**, pp. 3–22.

[38] C. N. Banwell, C. N. Banwell, *Fundamentals of molecular spectroscopy*, McGraw-Hill, **1994**.

[39] J. Raskó, *Journal of Catalysis* **2003**, *217*, 478–486.

[40] J. Farideh, *Structure of Hydrated Ions and Cyano Complexes by X-Ray Absorption Spectroscopy "Structure of Hydrated Ions and Cyano Complexes by X-Ray Absorption*, Prism 2000, **2000**.

[41] P. Carlsson, M. Skoglundh, *Applied Catalysis B: Environmental* **2011**, *101*, 669–675.

[42] P. Bazin, O. Saur, J. C. Lavalley, M. Daturi, G. Blanchard, *Physical Chemistry Chemical Physics* **2005**, *7*, 187–194.

[43] M. Happel, J. Mysliveček, V. Johánek, F. Dvořák, O. Stetsovych, Y. Lykhach, V. Matolín, J. Libuda, *Journal of Catalysis* **2012**, *289*, 118–126.

[44] L. DeRita, S. Dai, K. Lopez-Zepeda, N. Pham, G. W. Graham, X. Pan, P. Christopher, *Journal of the American Chemical Society* **2017**, *139*, 14150–14165.

[45] M. Kottwitz, Y. Li, R. M. Palomino, Z. Liu, G. Wang, Q. Wu, J. Huang, J. Timoshenko, S. D. Senanayake, M. Balasubramanian, D. Lu, R. G. Nuzzo, A. I. Frenkel, *ACS Catalysis* **(2019)**, *9*, 8738–8748.

[46] E. Becker, P. A. Carlsson, L. Kylhammar, M. A. Newton, M. Skoglundh, *Journal of Physical Chemistry C* **2011**, *115*, 944–951.

[47] S. K. Cheah, V. P. Bernardet, A. A. Franco, O. Lemaire, P. Gelin, *Journal of Physical Chemistry C* **2013**, *117*, 22756–22767.

[48] P. Carlsson, L. Österlund, P. Thormählen, A. Palmqvist, E. Fridell, J. Jansson, M. Skoglundh, *Journal of Catalysis* **2004**, *226*, 422–434.